Generic approach to assess the measuring performance of total-radiated power quantities by multi-channel resistive bolometer diagnostics on fusion experiments

L.C. Ingesson,[1,a] A. Doblas,[2] A. Gandhi,[3,b] S. Jahanbakhsh,[4] and H. Meister[4]

[1] Fusion for Energy, C/ Josep Pla 2, Torres Diagonal Litoral B3, 08019 Barcelona, Spain

[2] ATG, Plaça d'Ernest Lluch i Martin 5, 08019 Barcelona, Spain

[3] ADF Group, La Bastide Blanche – Bât G, 13127 Vitrolles, France

[4] Max Planck Institute for Plasma Physics (IPP), Boltzmannstr. 2, 85748 Garching, Germany

[a] Author to whom correspondence should be addressed: christian.ingesson@f4e.europa.eu

[b] Present affiliation: ATG, Plaça d'Ernest Lluch i Martin 5, 08019 Barcelona, Spain

ABSTRACT On present-day magnetic-confinement fusion experiments, the performance of multi-channel bolometer diagnostics has typically evolved over time through experience with earlier versions of the diagnostic and experimental results obtained. For future large-scale fusion experiments and reactors, it is necessary to be able to predict the performance as a function of design decisions and constraints.

A methodology has been developed to predict the accuracy with which the volume-integrated total radiated power can be estimated from the measurements by a resistive bolometer diagnostic, considering in particular its line-of-sight geometry, étendues of individual lines of sight, bolometer-sensor characteristics and the expected noise level that can be obtained with its electronics and signal chain. The methodology depends on a number of assumptions in order to arrive at analytical expressions, but does not restrict the final implementation of data-processing of the diagnostic measurements. The methodology allows to predict the performance in terms of accuracy, total-radiated power level and frequency or time resolution, and to optimize bolometer-sensor characteristics for a set of performance requirements. This is illustrated for the bolometer diagnostic that is being designed for the ITER experiment. The reasonableness, consequences and limitations of the assumptions are discussed in detail.

I. INTRODUCTION

On present-day magnetic-confinement fusion experiments, the performance of bolometer diagnostics, like other diagnostics, has typically evolved over time by diagnostic physicists and engineers recognizing opportunities for improvement based on experience with earlier versions of the diagnostic and experimental results obtained.[1,2] For future large-scale fusion experiments and reactors, it is necessary to be able to predict the performance as a function of design decisions and constraints. The required and predicted performance of measurement of a particular plasma parameter is typically expressed as the range of the parameter to be measured (dynamic range), the time resolution, the accuracy and, for spatially resolved measurements, the spatial resolution.[3,4] Also the required reliability and availability of the measurement of each parameter are important aspects, but outside the scope of this paper.

This paper describes a methodology that we have developed to predict the performance of the volume-integrated total radiated power (of the plasma overall or in specific regions) derived from measurements of a multi-channel bolometer diagnostic in terms of accuracy, time resolution and range. Although the methodology is generic for multi-channel resistive bolometer diagnostics on magnetic-confinement fusion experiments, it is illustrated for the bolometer diagnostic that is being designed for the ITER tokamak, an international fusion experiment under construction in southern France. Earlier work on the expected performance of the ITER bolometer diagnostic has focused on aspects such as predicting signal levels and the noise equivalent power of line-integral measurements that can be obtained, as well as the potential for optimization;[5] this paper builds on that work.

Section II describes the proposed methodology, considerations regarding the derivation of total radiated power from a set of bolometer lines of sight, two criteria for estimating the measurement performance of the total radiated power from the plasma from the bolometer measurements, and analytical expressions derived from those criteria. Section III uses those expressions to illustrate the performance achievable with a certain bolometer diagnostic (as being designed for ITER) and which diagnostic characteristics are needed to achieve a certain performance. Finally, limitations resulting from the assumptions made are considered in Sec. IV, with conclusions about the use of the methodology in Sec. V.

II. METHODOLOGY

The methodology is based on various considerations regarding system characteristics that determine the measurement performance. The key system characteristics that determine the measurement performance are the frequency-dependent sensitivity of the bolometer sensors, viewing geometry in terms of lay-out of its lines of sight, the étendue of the collimation and the noise level from signal chain and electronics. First, this section describes these

characteristics and the assumptions made for the proposed methodology. Then, equations are derived that allow estimates of the measuring performance.

A. Bolometer-sensor characteristics

On many magnetic-confinement fusion experiments bolometer sensors originally developed by Mast *et al.* are used.[6] A simple one-dimensional differential equation describes the relation between the incident light power $f(t)$ on the sensor as a function of time and the temperature change on the sensor $\Delta T(t)$ or output voltage $\Delta U_{\text{out}}(t)$ of the Wheatstone bridge in the sensor in very good approximation:[6]

$$f(t) = C\left(\frac{\mathrm{d}\Delta T(t)}{\mathrm{d}t} + \frac{\Delta T(t)}{\tau}\right) = \frac{2C}{\alpha U_{\text{in}}}\left(\frac{\mathrm{d}\Delta U_{\text{out}}(t)}{\mathrm{d}t} + \frac{\Delta\Delta U_{\text{out}}(t)}{\tau}\right), \tag{1}$$

where C is the heat capacity of the sensor (units J/K), τ the time constant of the heat conduction from the radiation-absorbing film to a heat sink (units s), and α the temperature coefficient of resistance of resistors that are the temperature-sensitive element in the sensors (units K^{-1}). The factor of two arises from the Wheatstone configuration to which a voltage U_{in} is applied, with two pairs of resistors behind two radiation-absorbing metal layers, one of which is exposed to plasma light (the signal absorber) and one of which is shielded from light (the reference absorber). When the signal absorber heats up as the result of incident radiation, the resistance values of one pair of resistors increase, causing a bridge imbalance that is measured as the output voltage (the output voltage is zero in a perfectly balanced bridge when there is no incident radiation). The bolometer is the thermal equivalent of an electrical RC circuit with a first-order response function in the angular frequency ω domain, the amplitude of which at frequency ω is given by:[7]

$$\frac{\widehat{\Delta U_{\text{out}}}'}{U_{\text{in}}} = S\hat{f}'\frac{1}{\sqrt{1+\omega^2\tau^2}}, \tag{2}$$

where the accent indicates quantities in the frequency domain, $S = \alpha\tau/2C$ is the sensitivity (units W^{-1}) and the hat over symbols indicates amplitudes of the quantity at a certain frequency or time. Equation (2) in the frequency domain is the amplitude part of the inverse of Eq. (1). Figure 1 illustrates some characteristic features of Eq. (2), in particular the attenuation above frequencies $\omega = 1/\tau$ or $\nu = 1/2\pi\tau$. If the characteristic noise density of the measurement is U_{noise}', a meaningful measurement is only obtained if

$$\widehat{\Delta U_{\text{out}}}' > U_{\text{noise}}'. \tag{3}$$

One can also consider the response of the bolometer sensor to a step in power $\hat{f}$ incident on the sensor after a time Δt, which is:

$$\frac{\widehat{\Delta U_{\text{out}}}}{U_{\text{in}}} = S\hat{f}\left(1 - e^{-\frac{\Delta t}{\tau}}\right). \tag{4}$$

This is the well-known step response of a first-order low-pass filter from control theory. Figure 2 illustrates some characteristic features of Eq. (4), including a characteristic level of noise U_{noise} in the measurement.
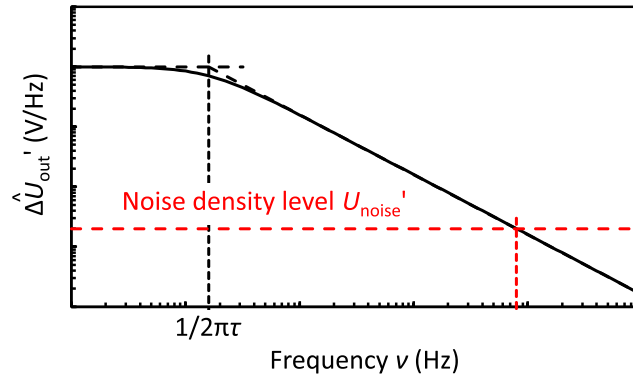
FIG. 1: The amplitude of the transfer function of the bridge voltage difference Eq. (2) as a function of frequency $\nu = \omega/2\pi$ on a log-log scale. Some characteristic points and slopes are shown, while the drop corresponds to the usual –6dB/octave of a first-order low-pass filter. A noise density level $\widehat{\Delta U_{\text{out}}}' = U_{\text{noise}}'$ is indicated by the horizontal dashed line (red in the online version).
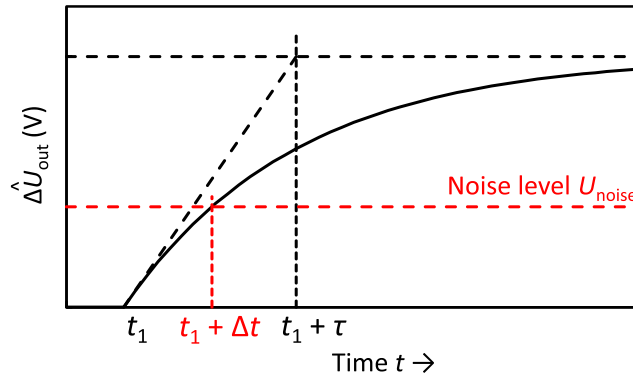
FIG. 2: The bridge voltage difference response to a step input power according to Eq. (4) as a function of time. Some characteristic points and slopes are shown. A noise level $\widehat{\Delta U_{\text{out}}} = U_{\text{noise}}$ is shown with a dashed line (red in the online version), with the corresponding achievable Δt indicted.

The noise level and how to relate it to measurable characteristics of the sensor require careful consideration. In a bolometer diagnostic, the noise is typically dominated by pick-up and interference along the measurement chain in the noisy environment of a fusion experiment in combination with long cables with many connections (e.g. electrical vacuum feedthroughs) and some unavoidable unshielded lengths of cable (with effects such as varying electrical fields, vibrations in magnetic field and microphonicity), rather than fundamental limits such as resistor or photon noise (which we quantify in Sec. III.A). To measure in such an environment, systems make use of the synchronous detection methodology with an AC voltage (with a frequency of the order of 10 kHz) applied to the Wheatstone bridge, which rejects the noise outside a window of 0.1–1 kHz around the AC frequency. Within this narrow window (e.g. 10±1 kHz) the noise is likely to be reasonably constant, which is the reason for the assumption of a constant noise

density spectrum in Fig. 1 and the following derivations (i.e. assumption that noise is 'white'). From Eq. (1) and the definition of sensitivity, we can define the noise-equivalent power of a bolometer channel with sensor sensitivity S as $\text{NEP}_f = U_{\text{noise}}/SU_{\text{in}}$, where the subscript f indicates that it is related to the incident light power on the sensor of Eq. (1). Note that in a bolometer diagnostic the output voltage is proportional to light power, which is in contrast to normal signal-processing theory of electrical signals where the power is proportional to the square of the voltage.

Prototype bolometer sensors for ITER have been calibrated to give the temperature-dependent sensitivity S and time constant τ,[8] which will be used in the examples of achievable performance in this paper (see Sec. III.A for a description of the sensors). The NEP_f for channels with sensors with sensitivity S has not been characterized; instead it has been scaled from the sensitivity of a reference sensor S_{ref} for which $\text{NEP}_{f,\text{ref}}$ is known by:

$$\text{NEP}_f = \text{NEP}_{f,\text{ref}}\, S_{\text{ref}}/S. \tag{5}$$

Thus, a channel with a sensor that is more sensitive will effectively experience less noise. The experimental characterization of the NEP_f did not consider the spectral density. Here it is assumed that an equivalent synchronous detection system (noise characteristics, bandwidth and U_{in}) is used for the sensors under consideration and the reference system, i.e. so that $\text{NEP}_{f,\text{ref}}$ and NEP_f are comparable.

To use criterion Eq. (3) for noise density level, we will simply assume that the attenuated amplitude of the power $\hat{f}$ incident on the sensor at frequency ω is measurable if

$$\hat{f} > \frac{\sqrt{1+\omega^2\tau^2}}{SU_{\text{in}}}\widehat{\Delta U_{\text{noise}}} = \sqrt{1+\omega^2\tau^2}\,\text{NEP}_f. \tag{6}$$

This derivation uses Eq. (2) and the relation between NEP_f and U_{noise} above, but ignores the spectral density aspect. The consequences and applicability of the criterion in Eq. (6) will be further considered in Sec. IV. A similar criterion can be derived from the step response of Eq. (4), where the noise level is that in the time domain. From Fig. 2 and using the same relation between NEP_f and U_{noise} above one can conclude that the response is measurable if the step size $\hat{f}$ and duration of the step Δt satisfy

$$\hat{f} > \frac{1}{SU_{\text{in}}\left(1-e^{-\frac{\Delta t}{\tau}}\right)}\widehat{\Delta U_{\text{noise}}} = \frac{1}{\left(1-e^{-\frac{\Delta t}{\tau}}\right)}\text{NEP}_f. \tag{7}$$

B. Viewing geometry

Bolometer tomography diagnostics view a poloidal cross-section of the plasma and measure the emitted radiation along a number of lines of sight by means of collimated views from bolometer sensors.[1] Sometimes, the lines of sight are in different poloidal cross-sections, but, if toroidal symmetry is a valid assumption, they can be overlaid in one poloidal plane. The

methodology and examples in this paper assume a number of lines of sight as in Fig. 3, a subset of which was used in the analysis as described in Sec. III.A. The distribution of lines-of-sight and pinholes and collimators of the ITER bolometer diagnostic are based on best-practice from present-day fusion experiments, constraints of the ITER project (such as interfaces with other systems and number of electrical cables available) and past performance analysis, the optimization of which has been described elsewhere.[5]

The collimator and pin-hole geometries define viewing cones around the line of sight of each channel. The étendue (or throughput of an optical system, in units $sr\,m^2$) allows the measurement of a finite beam width to be considered as line integral. The measured power of channel i, f_i (in W), can be converted to the line-integral value $\widetilde{f}_i$ by

$$\widetilde{f}_i = 4\pi f_i/e_i \; [W/m^2], \tag{8}$$

where e_i [$sr\,m^2$] is the étendue of the channel while isotropic emission from the optically thin plasma (expressed in W/m^3) is assumed.[9]
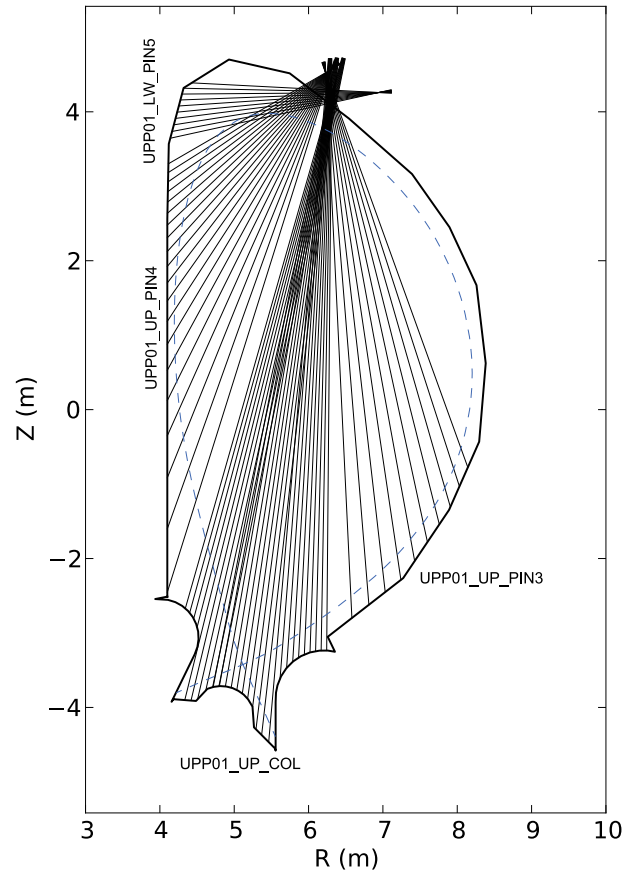

FIG. 3: Lines of sight from bolometer cameras in the upper port on ITER, relevant for the examples given in this paper, overlaid in a poloidal cross-section of the ITER first wall in the vacuum vessel. The cameras are identified with the names as in Table II. This corresponds to a subset of all the cameras of the diagnostic.[5] The dashed line (blue in the online version) indicates the typical extent of the plasma.

6

C. Estimation of total radiated power

There are various ways in which the total radiated power can be derived from bolometer line-of-sight measurements, for example by post-processing of tomographic reconstructions, by weighted-sum approximation (used extensively,[10,11] and reviewed in Ref. 12), or neural networks.[13] The weighted-sum approximation is the most straightforward, has a simple geometric interpretation, and allows an analytical expression of a representative estimate of the accuracy in view of measurement errors, which is why we have used it in the methodology. Considerations regarding the weighted-sum approximation being representative are discussed at the end of this subsection. As described in Sec. III.B, the line-integral values $\tilde{f}_i$ [W/m^2] are obtained from the measured power f_i of channel i (expressed in watt) by means of Eq. (8). For parallel vertical lines of sight with a spacing Δp_i and toroidally symmetric emissivity, the total radiated power can be calculated by

$$P_{\text{rad}}[W] = 2\pi R_0 \sum_i \tilde{f}_i \Delta p_i = \sum_i b_i \tilde{f}_i, \qquad (9)$$

where R_0 is the major radius of the torus and $b_i = 2\pi R_0 \Delta p_i$. The interpretation is that this is a numerical integral over the entire plasma volume: the factor $2\pi R_0$ representing the toroidal integral, the line integrals along vertical lines of sight representing the integral in vertical direction, and Eq. (9) the numerical integral in radial/horizontal direction.[12] The same expression can be used as an approximation even if the lines of sight are not vertical and not parallel, such as in Fig. 3; the spacing Δp_i is then to be interpreted as the average distance between lines of sight, or the distance weighted by the emission level along the lines of sight. Finally, the expression can also be used for non-continuous sets of lines of sight, in which case b_i in Eq. (9) are coefficients that do not have a geometrical interpretation, and are simply fitting parameters for each channel i in the set.[11] In the case of non-vertical lines of sight, the optimum fitting parameters are obtained by statistical analysis on a training set of profiles representing a wide range of emission profiles.[10,11]

The error in the derived total radiated power of Eq. (9) resulting from random measurement errors (noise) in the line-integral measurements $\Delta \tilde{f}_i$ can be expressed, assuming that the noise between channels is uncorrelated and it being the only source of errors, as

$$\Delta P_{\text{rad}}[W] = 2\pi R_0 \sqrt{\sum_i (\Delta \tilde{f}_i \Delta p_i)^2} = \sqrt{\sum_i (b_i \Delta \tilde{f}_i)^2}. \qquad (10)$$

It can be noted that the line-integral NEP of the sensor $\Delta \tilde{f}_i = 4\pi \text{NEP}_f / e_i$ is obtained according to Eq. (8). The quantity ΔP_{rad} of Eq. (10) can also be understood as a noise-equivalent-total-power, where the total power is that emitted by a given volume of the plasma (which is of the order of MW, in contrast to the noise equivalent power NEP_f of a channel, which is of the order of μW–mW). In case the weights Δp and noise level $\Delta \tilde{f}$ are the same for all N channels, the expression simplifies to $\Delta P_{\text{rad}}[W] = 2\pi R_0 \Delta \tilde{f} \Delta p \sqrt{N}$. For a consistent weighted sum for

different numbers of channels, Δp must be inversely proportional to N. This implies that the relative error $\Delta P_{rad}/P_{rad}$ will typically be a factor of $1/\sqrt{N}$ of $\Delta \tilde{f}/\tilde{f}$, i.e. scaled by the familiar factor $1/\sqrt{N}$. This further simplification is useful for theoretical insight, but is not used in the methodology, which instead uses Eq. (10).

We expect the error in derived total radiated power in Eq. (10) according to the weighted-sum approximation also to be representative of other methods to calculate the total radiated power (e.g. from tomographic reconstructions, neural networks, or from different combinations of lines of sight). This is because all calculations of total emitted power from line integrals will involve a similar integral operator as in Eq. (9) and thus the noise propagation to be according to Eq. (10). As observed in the previous paragraph, the noise propagation scales with a factor of $1/\sqrt{N}$. If the method uses many lines of sight N, as is typically the case with tomography, the errors will thus be correspondingly smaller (not necessarily related to local values having been obtained by regularization).

D. Criteria and equations for performance estimate

A key assumption in the methodology is that the emission profile does not change shape, only magnitude: i.e. plasma emissivity is assumed to scale linearly with total radiated power according to the fixed profile shape. With this assumption, the linearity of Eq. (9) and provided all sensors are the same (all have the same τ), $\tilde{f}_i$ scale proportionally with P_{rad}, and the measured power $\hat{f}$ and noise-equivalent power NEP_f for the channel in the criteria of Eqs. (6) and (7) can be replaced by $\widehat{P_{rad}}$ and ΔP_{rad}, respectively. However, the term ΔP_{rad} needs to be replaced by $\Delta P_{rad}/\gamma\beta$, because to achieve a certain relative accuracy β in the derived total radiated power the signal must not just be larger than the ΔP_{rad} that is given by the noise level, but exceed it sufficiently to achieve that accuracy. We use 'accuracy' as the measure of closeness of the measurement (such as the derived total radiated power) to its true value, involving both random and systematic errors. Here, γ is the fraction of the total error that results from random line-integral power signal noise [i.e. the part of the measurement error that contributes to Eq. (10)], while the rest $(1 - \gamma)$ results from other random and systematic errors as well as other sources of uncertainties in the derivation model, such as the weights in the weighted summation not being perfect, the calibration not being perfect or temperature-dependent calibration factors having to be applied at imperfectly known sensor temperature, imbalances of the Wheatstone bridge (from intrinsic to temperature-gradient induced imbalance), attenuation in the transmission line that is not corrected for perfectly, imperfect knowledge of the viewing geometry, toroidal asymmetries playing a role if the viewing geometry is not in one poloidal cross-section, thermal radiation from the surroundings of the sensor, and effects not taken into account in the analysis (such as plasma light reflected by the wall reaching sensors, charge-exchange neutrals from the plasma making a contribution to the bolometer measurement, or some degree of optical thickness of the plasma). In the examples

that will be given, we assumed the requirement that P_{rad} must be derived with a relative accuracy of $\beta = 10\%$ and an arbitrary $\gamma = 0.5$. This implies that the diagnostic must have been designed and characterized to the extent that all other sources of errors and uncertainties contribute less than $(1 - \gamma)\beta = 5\%$. The reasonableness of this assumption is discussed in more detail in Sec. IV.

With this approach, Eqs. (6) and (7) translate to the following criteria for the total radiated power:

$$\widehat{P_{rad}} > \frac{\sqrt{1+\omega^2\tau^2}\Delta P_{rad}}{\gamma\beta},$$ (11)

and

$$\widehat{P_{rad}} > \frac{1}{\left(1-e^{-\frac{\Delta t}{\tau}}\right)}\frac{\Delta P_{rad}}{\gamma\beta},$$ (12)

respectively. An alternative interpretation of Eq. (11) is that because all sensors are equal, the frequency component at frequency ω of measured signals is attenuated by $1/\sqrt{1+\omega^2\tau^2}$, and thus that the frequency component of the total radiated power at frequency ω must be a factor $\sqrt{1+\omega^2\tau^2}$ larger to achieve the same signal magnitude as at $\omega = 0$, i.e. constant P_{rad}.

It can be noted that Eqs. (11) and (12) link exactly the three aspects that constitute a requirement for a measurement parameter mentioned in Sec. I: range (in this case $\widehat{P_{rad}}$, with the minimum achievable given by the equations), the relative accuracy β and the time resolution Δt (or the closely related frequency $\nu = \omega/2\pi$).

If all sensors are the same, with Eqs. (5) and (8),

$$\Delta\tilde{f}_i = 4\pi NEP_f/e_i = 4\pi NEP_{f,ref}\, S_{ref}/e_i S,$$ (13)

and thus with Eq. (10):

$$\Delta P_{rad} = 2\pi R_0\sqrt{\Sigma_i\left(\Delta\tilde{f}_i\Delta p_i\right)^2} = 8\pi^2 R_0 NEP_{f,ref}\frac{S_{ref}}{S}\sqrt{\Sigma_i\left(\frac{\Delta p_i}{e_i}\right)^2} =$$

$$\Delta P_{rad,ref}\frac{S_{ref}}{S} = \frac{G\times NEP_{f,ref}}{S},$$ (14)

which is a fixed value for a given set of weighted-sum parameters, étendues, $NEP_{f,ref}$ and sensor sensitivity. Here, $\Delta P_{rad,ref} = 8\pi^2 R_0 NEP_{f,ref}\sqrt{\Sigma_i(\Delta p_i/e_i)^2} = 4\pi NEP_{f,ref}\sqrt{\Sigma_i(b_i/e_i)^2}$. To be able to compare different sensors and different $NEP_{f,ref}$, it is convenient to introduce a geometric factor G in Eq. (14):

$$G = 8\pi^2 R_0 S_{ref}\sqrt{\Sigma_i(\Delta p_i/e_i)^2} = 4\pi S_{ref}\sqrt{\Sigma_i(b_i/e_i)^2}.$$ (15)

Thus, Eq. (14) and the factor G from Eq. (15) contain all relevant quantification about the diagnostic (apart from the factor γ) to link it through ΔP_{rad} to the measurement requirement as expressed in Eqs. (11) and (12). Resulting expressions to describe the measuring performance of the diagnostics are explored next.

For the first criterion, using Eq. (14), Eq. (11) becomes

$$\widehat{P_{\text{rad}}} > \frac{\sqrt{1+\omega^2\tau^2}\,G\times\text{NEP}_{f,\text{ref}}}{\gamma\beta S} = \widehat{P_{\text{rad,noise}}}\sqrt{1+\omega^2\tau^2}, \tag{16}$$

where

$$\widehat{P_{\text{rad,noise}}} = \frac{G\times\text{NEP}_{f,\text{ref}}}{\gamma\beta S} \tag{17}$$

represents the minimum that can be measured, given by Eq. (16) at $\omega = 0$.

Solving Eq. (16) for frequency ω gives

$$\omega < \frac{\sqrt{\left(\frac{\gamma\beta S\widehat{P_{\text{rad}}}}{G\times\text{NEP}_{f,\text{ref}}}\right)^2 - 1}}{\tau} = \frac{\sqrt{\left(\frac{\widehat{P_{\text{rad}}}}{\widehat{P_{\text{rad,noise}}}}\right)^2 - 1}}{\tau}, \tag{18}$$

while solving it for relative accuracy β gives

$$\beta > \frac{G\times\text{NEP}_{f,\text{ref}}}{\gamma S\widehat{P_{\text{rad}}}}\sqrt{1+\omega^2\tau^2}. \tag{19}$$

Sensors with a sensitivity S as a function of time constant that satisfy

$$S > \frac{\sqrt{1+\omega^2\tau^2}\,G\times\text{NEP}_{f,\text{ref}}}{\gamma\beta\widehat{P_{\text{rad}}}}. \tag{20}$$

will be able to measure a power $\widehat{P_{\text{rad}}}$ with frequency ω and relative accuracy β.

Following the same approach for the alternative criterion, Eq. (12) becomes

$$\widehat{P_{\text{rad}}} > \frac{1}{\left(1-e^{-\frac{\Delta t}{\tau}}\right)}\frac{G\times\text{NEP}_{f,\text{ref}}}{\gamma\beta S} = \frac{\widehat{P_{\text{rad,noise}}}}{\left(1-e^{-\frac{\Delta t}{\tau}}\right)}. \tag{21}$$

The lowest power $\widehat{P_{\text{rad,noise}}}$ that can be measured (for $\Delta t \gg \tau$) is the same Eq. (17) as for the other criterion. Solving Eq. (21) for time step Δt gives

$$\Delta t > -\tau\ln\left(1 - \frac{G\times\text{NEP}_{f,\text{ref}}}{\gamma\beta S\widehat{P_{\text{rad}}}}\right) = -\tau\ln\left(1 - \frac{\widehat{P_{\text{rad,noise}}}}{\widehat{P_{\text{rad}}}}\right), \tag{22}$$

while solving it for relative accuracy β gives

$$\beta > \frac{1}{\left(1-e^{-\frac{\Delta t}{\tau}}\right)}\frac{G\times\text{NEP}_{f,\text{ref}}}{\gamma S\widehat{P_{\text{rad}}}}. \tag{23}$$

Sensors with a sensitivity S as a function of time constant that satisfy

$$S > \frac{1}{\left(1-e^{-\frac{\Delta t}{\tau}}\right)} \frac{G \times \text{NEP}_{f,\text{ref}}}{\gamma \beta \widehat{P_{\text{rad}}}}. \tag{24}$$

will be able to measure a power $\widehat{P_{\text{rad}}}$ with time step Δt and relative accuracy β.

III. ANALYSIS

A.   Inputs to the analysis

The prototype bolometer sensors compared in this paper, and the reference sensor for which $\text{NEP}_{f,\text{ref}}$ has been determined, consist of a 3-μm thick silicon-nitride membrane that is supported by a 0.6-mm thick silicon structure that acts as heat sink. The resistors on the reference and prototype sensors were of identical construction. The absorber in the case of the reference sensor was 12-μm thick Pt,[5] while for the prototype sensors it was 20-μm thick Au.[8] The absorber size that receives light is 1.5×4.0 mm^2. A metal heat conduction layer (HCL) between the absorber and heat sink can increase the heat flow with respect to only the silicon-nitride membrane. The composition and thickness of the HCL can be used to tailor the sensitivity and time constant of the sensor. The transfer time through the membrane (i.e. between absorber and resistors) theoretically is shorter than 0.1 ms and thus is generally considered negligible, although the sensor response to millisecond-scale events is an aspect of active consideration. The characteristics of the reference and three prototype sensors (with different HCL thicknesses) are given in Table I and are shown graphically in Fig. 6. For the prototype sensors, S/τ varies less than 2.6% between the three HCL thicknesses, the consequences of which are discussed in Sec. B. It can be noted that the sensitivity of the sensors strongly decreases with temperature,[8] which is the explanation for the higher sensitivity of the reference sensor for comparable τ in Fig. 6, which was calibrated at room temperature with respect to the prototype sensors at 200°C, which is more representative of the operational conditions of the bolometer sensors in ITER.

For the reference sensor, $\text{NEP}_{f,\text{ref}} = 1$ μW had been established in laboratory conditions,[5] which we consider the best available estimate. A small fraction of $\text{NEP}_{f,\text{ref}}$ results from thermal resistor noise, while photon noise is negligible. The resistor noise generates a voltage $\sqrt{4k_{\text{B}}TRB}$, where k_{B} is the Boltzmann constant, T the maximum operating temperature of the sensor (corresponding to 350°C), R the Wheatstone bridge at that temperature (of the order of 2 kΩ), and B the bandwidth of the synchronous detection system (2 kHz). This voltage is measured by the bolometer diagnostic as a power $\text{NEP}_{\text{resistor}} \sim 0.3$μW, where a conservative driver voltage and sensor sensitivity are assumed, thus well below the experimentally determined $\text{NEP}_{f,\text{ref}}$. The photon noise is negligible by many orders of magnitude because the experimentally determined $\text{NEP}_{f,\text{ref}}$ corresponds to at least 10^9 photons/s in the relevant photon-energy range, i.e. far too large for photon statistical effects to be noticeable.

Table I Experimentally determined characteristics of the reference and three prototype sensors used. Of the temperature-dependent calibration done of the prototype sensors, the temperature closest to a representative operating temperature of 200°C were taken. The tolerance of the sensitivity and time constant is the typical standard deviation from repeated calibrations and variation of calibration factors between the signal and reference parts of the sensor.

	Reference	Sensor 1	Sensor 2	Sensor 3
Heat-conduction layer (HCL)	150 nm Al	0 nm (none)	200 nm Pt	350 nm Pt
Characterization temperature (°C)	26	204	200	200
Sensitivity S (W^{-1})	0.79 ± 0.01	1.25 ± 0.01	0.765 ± 0.007	0.553 ± 0.007
Time constant τ (s)	0.314 ± 0.006	0.816 ± 0.008	0.522 ± 0.010	0.372 ± 0.013

Table II Line-of-sight (LOS) parameters for a selection of lines of sight of the ITER bolometer diagnostic shown in Fig. 3 as used in the examples given in this section.

Camera identifier	Number of LOS in calculation	Effective étendue e_i ($\times 10^{-9}$ sr m^2)	Average LOS distance (m)	Coefficients b_i (m^2)	Typical signal f_i (mW)	Line integral $\widetilde{f_i}$ (MW/m^2)	$\Delta\widetilde{f_i}$ for reference sensor (kW/m^2)
UPP01_LW_PIN5 (10 channels)	4	4.2	0.125	4.5	0.009	0.027	3.03
UPP01_UP_PIN4 (20 channels)	8	14.0	0.313	11.3	0.2	0.18	0.90
UPP01_UP_COL (30 channels)	24	3.6	0.063	2.3	0.15	0.52	3.49
UPP01_UP_PIN3 (10 channels)	4	10.3	0.375	13.6	0.3	0.37	1.22

Table II lists the line-of-sight parameters for a selection of lines of sight from Fig. 3. The selection in Table II takes into account that the ITER bolometer diagnostic needs to provide a number of redundant estimates of the total radiated power (i.e. from multiple subsets of lines of sight, at least two subsets from the lines of sights in Fig. 3), and a number of lines-of-sight blinded to provide a reference measurement to be able to account for operation at variable temperatures that induce thermal gradients over the sensors. The selection of lines of sight determines in particular the average distance between lines of sight Δp_i and coefficients b_i. The typical signals f_i and étendues in Table II are from Ref. 5, from which the line-integral values $\widetilde{f_i}$ have been calculated with Eq. (8). The étendue takes into account a grid to attenuate mm-wave radiation that could affect the bolometer-sensor measurements, in particular stray radiation from the electron-cyclotron resonance heating system.[14] The grid has a 50% transmission in the photon-energy range relevant for the bolometer measurement. Similarly, using the étendues, the line-integral noise-equivalent power $\Delta\widetilde{f_i}$ for the reference sensor have been calculated from $NEP_{f,\mathrm{ref}}$ in table II using the first expression in Eq. (13). The coefficients b_i in table II have been scaled by a factor of 0.96 to match the total radiation power of the profile that had been used to calculate the synthetic measurements (65 MW) – this factor is a

correction for the b_i calculated with the average LOS distance in table II to account for weighting by the emission profile shape and diverging (non-parallel) lines of sight.

From the values in table II, one can calculate the total radiated power from the weighted sum Eq. (9) (65 MW), $\Delta P_{rad,ref}$ according to Eq. (14) (64.5 kW) and the geometric factor G according to Eq. (15) (5.10×10^{10} W^{-1}).

In the following, we refer to frequency ω (or $\nu = \omega/2\pi$ in the figures) in the context of the transfer function of Eq. (2). With the Nyquist theorem, one can determine a suitable sampling rate to measure a particular frequency. However, the inverse of frequency ν does not necessarily equate meaningfully to the notion of time resolution. We will therefore only refer to time resolution Δt as the time step that is above the noise level in the context of the criterion based on the step response of Eq. (4) or Eq. (22).

B.   Measurement parameters: dependence on range, accuracy and time resolution

If Eqs. (16) and (21) are converted to equalities, they define a manifold (surface) in the frequency-$\widehat{P_{rad}}$-accuracy space (ν-$\widehat{P_{rad}}$-β space), and time-resolution-$\widehat{P_{rad}}$-accuracy space (Δt-$\widehat{P_{rad}}$-β space), respectively. The inequality in Eqs. (16) and (21) then expresses which side of the manifold satisfies the criterion. Although it is possible to make a three-dimensional plot of the manifolds, it is easier to read the quantification if cross-sections are plotted.

Figures 4(a,b) show ν and Δt as function of $\widehat{P_{rad}}$ for fixed β, as given by Eqs. (18) and (22), for the three bolometer-sensor prototypes described in Table I. The overall shape of the curves for frequency follow $\sqrt{1 + \omega^2\tau^2}$ of Fig. 1, which determines the asymptotic limit that increases linearly on log-log scale (i.e. a factor of 10 increase in power makes it possible to measure at 10 times higher frequency, which results from the –6dB/octave drop of the sensor attenuation curve as a function of frequency), and the bend at lower $\widehat{P_{rad}}$. Because S/τ is approximately the same for the three sensors, the asymptote for high $\widehat{P_{rad}}$ approximately overlaps – in (a) the asymptote for sensor 1 based on the derivative of Eq. (18) is shown (dotted line, green in the online version). At low $\widehat{P_{rad}}$, however, the shape varies, characterized by τ (horizontal lines on the left side, blue in the online version). The lowest power measurable $\widehat{P_{rad,noise}}$ of Eq. (17) is clearly discernable (dotted vertical line for sensor 1, red in the online version), which in effect is at frequency $\omega = 0$ or time resolution $\Delta t \to \infty$. If other parameters than the sensor time constant change (G, NEP$_{f,ref}$, γ, β and S) it leads to a change of $\widehat{P_{rad,noise}}$ (e.g. it is inversely proportional with S), which results in a shift left or right of the curve. The inverse of the curves for time resolution have a very similar shape.

Figure 5 shows ν as a function of β for a number of fixed $\widehat{P_{rad}}$ for one sensor prototype, also according to Eqs. (18), which complements Fig. 4(a) to give insight in the behavior and rate of change in the entire parameter space. The variation of accuracy is relatively weak compared to

13

the variations in Fig. 4(a). Expression (19) describes the inverse of the plot in Fig. 5, i.e. β as a function of ω, which can be used to find the achievable accuracy for given other parameters. Similar plots can be made for Δt as function of β according to the second criterion of Eqs. (22) and (23) – note that Eq. (22) has a greater-than sign in contrast to the less-than sign in Eq. (18). The relative accuracy at $\omega = 0$ or at $\Delta t \to \infty$ is $\beta > G \times \mathrm{NEP}_{f,\mathrm{ref}}/\gamma S \widehat{P}_{\mathrm{rad}}$.

The combination of Figs. 4 and 5 can be used to quantify the performance of a bolometer diagnostic, for example whether a measurement requirement as given by the points in Fig. 4 is satisfied.
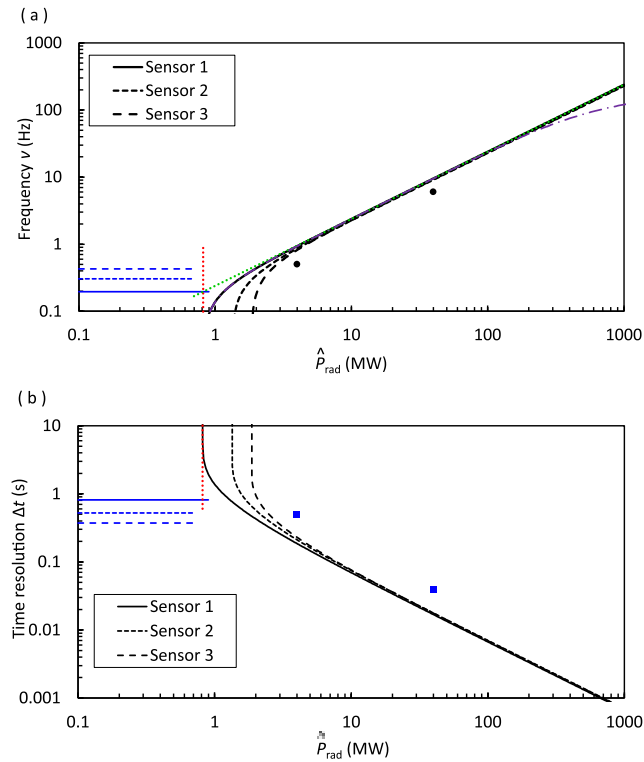

FIG. 4: Cross-section of the manifolds for fixed relative accuracy $\beta = 10\%$ for the three prototype sensors described in Table I (solid, dashed and long-dashed curves). (a) Frequency v as function of $\widehat{P}_{\mathrm{rad}}$ according to Eq. (18), with points in parameter space below the curve satisfying the criterion. (b) Time resolution Δt as function of $\widehat{P}_{\mathrm{rad}}$ according to Eq. (22), with points in parameter space above the curve satisfying the criterion. For all sensors the corresponding values $v = 1/2\pi\tau$ and τ are shown as horizontal lines on the left side with corresponding linestyle (in blue in the online version). The value of $\widehat{P}_{\mathrm{rad,noise}}$ of Eq. (17), which corresponds to the lowest $\widehat{P}_{\mathrm{rad}}$ measurable, is shown for sensor 1 as a vertical dotted line (red in the online version). The asymptote for $\widehat{P}_{\mathrm{rad}} \to \infty$ is also shown as a dotted line in (a) (green in the online version). The dot-dashed line in (a) (purple in the online version), which deviates from the other curves at high frequencies, corresponds to application of a 10-point rectangular filter average with a sampling rate of 1 kHz to the measured voltages in Eq. (1) as described in Sec. IV [because of the frequency dependence of the filter function, this curve was evaluated as P_{rad} against frequency from Eq. (16) rather than as frequency against P_{rad} according to Eq. (18) as the other curves]. Each figure shows two points $(\widehat{P}_{\mathrm{rad}}, v)$ and $(\widehat{P}_{\mathrm{rad}}, \Delta t)$ that are considered further in Fig. 6.
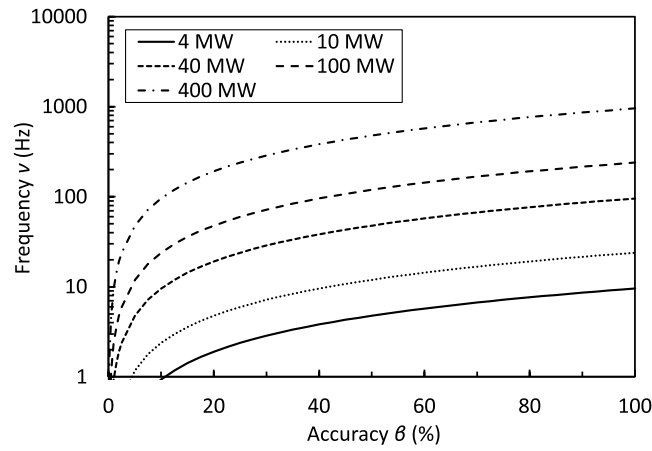
FIG. 5: Cross-section of manifold for five constant $\widehat{P_{rad}}$ values for prototype sensor 1 in Table I, with frequency ν as function of β according to Eq. (18), with points in parameter space below the curve satisfying the criterion (less-than symbol in the equation).

C.   Sensor optimization

Provided the assumption expressed in Eq. (5) is at least approximately correct, i.e. that the noise equivalent power of a sensor scales with the inverse of the sensitivity with respect to that of the reference sensor, one can consider the range of bolometer sensor properties that would satisfy one or more requirements resulting from operational needs expressed as individual points $(\widehat{P_{rad}}, \nu, \beta)$ or $(\widehat{P_{rad}}, \Delta t, \beta)$, by means of Eqs. (20) and (24), respectively. For illustration, bolometer-sensor sensitivities and time constants that would just satisfy a requirement are shown in Fig. 6 for a number of arbitrarily chosen points (i.e. the points shown in Fig. 4). For insight, Fig. 6 shows the asymptotes for one curve as an example. Although a zero time constant is not achievable in reality, analyzing it provides insight: for the first criterion [Eq. (20)], each curve (black in the online version) has a horizontal intersection $S = G \times \mathrm{NEP}_{f,ref}/\gamma \beta \widehat{P_{rad}}$ at $\tau = 0$ (dotted horizontal line; red in the online version). For the second criterion Eq. (24) (blue curves in the online version), the same values are reached close to $\tau = 0$, but there is a singularity. The slope of Eq. (20) for $\tau \rightarrow \infty$ is proportional to $\omega/\widehat{P_{rad}}$ and the asymptote (slanted dotted line; green in the online version) goes through the origin; the bend is around $\tau = 1/\omega$ (vertical dotted line; red in the online version). With these dependences on $\widehat{P_{rad}}$ and ω, it is clear that a wide range of curves with different intersection at $\tau = 0$ and slopes can be obtained depending on the choice of the $(\widehat{P_{rad}}, \nu, \beta)$ or $(\widehat{P_{rad}}, \Delta t, \beta)$ requirements.

The value of the representation in S-τ space is that various $(\widehat{P_{rad}}, \nu, \beta)$ or $(\widehat{P_{rad}}, \Delta t, \beta)$ requirements can be combined in the same figure and one can see compliance at one glance. It is possible to consider requirements for other measurement parameters in the same plot, creating an ensemble of curves. Examples of other measurement parameters are the total radiated power in different regions of the plasma than the total of the entire cross section, such as separately in the divertor and in the main plasma, which would be obtained from weighted summation of different views and numbers of lines of sight, and thus with different factors G.

Sensors that lie above the compound curve of the ensemble of all curves in the plot would comply with all the imposed requirements.

A figure like Fig. 6 can help to choose the most appropriate sensor characteristics among the possibilities, such as the optimum HCL thickness in our case. One can note that prototype sensors with different HCL shown in Fig. 6 lie on a curve (not drawn) with a slope comparable with the $S\text{-}\tau$ curves of the selected $(\widehat{P_{\mathrm{rad}}}, V, \beta)$ or $(\widehat{P_{\mathrm{rad}}}, \Delta t, \beta)$ requirements. Although it of course depends strongly on the particular $(\widehat{P_{\mathrm{rad}}}, V, \beta)$ or $(\widehat{P_{\mathrm{rad}}}, \Delta t, \beta)$ requirements, a number of general observations can be made. On the basis of the representation in Fig. 4, one might have concluded that the sensor with highest sensitivity (without HCL) is always best because it allows to measure the smallest signals (while at high powers and frequencies the sensors perform equally). However, Fig. 6 shows that the situation is more nuanced and there is less benefit in high sensitivity: although in this particular case the sensor with highest sensitivity is furthest above the curves (which gives the largest margin regarding performance), because of the overall slopes of the curves the difference is less pronounced than one might have thought. This means that other considerations may decide on the preferred HCL thickness, such as its robustness, careful consideration of the maximum temperature rise that the sensor will experience from various signals (high frequency, pulse response, etc.) and the need for a finite-thickness HCL to allow an electrical connection to the sensor absorber to avoid that it floats electrically and could get charged. Figure 6 would also show the impact of other sensor design aspects that could be varied, such as dimension and material choice. An optimized sensor or range of them can then again be plotted as one or more curves as in Fig. 4. For ITER, it does not seem appropriate nor necessary to extend the range of $S\text{-}\tau$ values beyond that represented by sensors 1 and 3. The sensitivity cannot be improved (and time constant extended) beyond that of sensor 1 (without HCL) without reducing the membrane thickness and thus affecting robustness negatively. The Pt HCL thickness of sensor 3 already affects its robustness. Although it is possible to replace it by more conducting materials such as gold or aluminum to shorten the time constant, Fig. 6 suggests there is little benefit in shortening the time constant beyond that of sensor 3 as there would be less margin with respect to the curves. Experimental testing of robustness of prototype sensors against various environmental factors is ongoing.
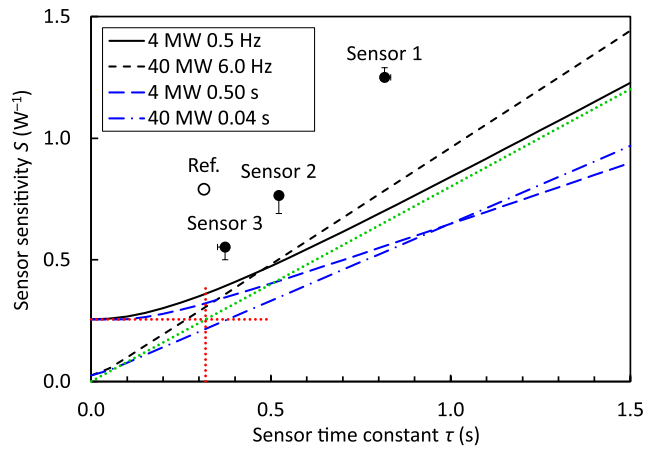
FIG. 6: Curves in S-τ space of sensors that have curves in v-$\widehat{P_{rad}}$-β or Δt-$\widehat{P_{rad}}$-β space that go through the parameter-space points $(\widehat{P_{rad}}, v, \beta)$ and $(\widehat{P_{rad}}, \Delta t, \beta)$ that are indicated as points in Fig. 4 (which is for relative accuracy $\beta = 10\%$). The solid and dashed curves (black in the online version) correspond to the frequency criterion [Eq. (20), Fig. 4(a)], and the long dashed and dot-dashed curves (blue in the online version) to the step-function criterion [Eq. (24), Fig. 4(b)]. Sensors with sensitivity and time constant above a curve would satisfy the criterion. For one of the curves (corresponding to 4 MW, 0.5 Hz and 10%), the asymptotes and $\tau = 1/2\pi v$ are drawn as dotted lines. The actual prototype sensors (solid circles) and the reference sensor (open circle) from Table I are shown for information, which the error bars indicating the range of calibration values found for various sensors with the three different HCL thicknesses (4 to 8 sensors of each thickness), which is indicative of the variation that can be expected in manufactured sensors.

IV. DISCUSSION ON ASSUMPTIONS

The methodology providing analytical expressions, and quantitative measurement performance predictions by it, are dependent on the validity and degree of correctness of the assumptions made. Each of the assumptions and any resulting limitations are discussed in turn next: sensor characteristics being identical for each line of sight, the noise equivalent power scaling with the inverse of the sensor sensitivity with respect to a reference sensor, noise being white and uncorrelated between different sensors and other considerations regarding the noise equivalent power, the filter function needed to evaluate Eq. (1), the shape of the emission profile being fixed, sources of uncertainties in the measuring system affecting the achievable accuracy (in particular the factor γ), Eq. (1) being a good approximation of bolometer-sensor behavior, and the weighted-sum approach being representative. As will be argued in Sec. V, the methodology can still provide useful insights even if not all assumptions are fully valid.

Two related assumptions are that all lines of sight used have identical sensors, i.e. the same sensitivity, time constant and noise equivalent power, and that for different incarnations of the sensor (different HCL thicknesses) the noise equivalent power scales with the inverse of the sensor sensitivity with respect to a reference sensor according to Eq. (5). The former assumption is not needed for actual application of the weighted sum approach to derive plasma parameters from measurements – it simply is needed for achieving the analytical expressions in Sec. II.D. Sensors with different τ will have a different attenuation at a given frequency ω

according to Eq. (2), and also different signal chains will introduce different noise levels for different lines of sight, for example when a range of different cable lengths and routings are used. Thus, normally, the weighted sum will mix many different frequency responses – by assuming it to be the same for all lines of sight, the attenuation for a certain frequency also applies the total radiated power according to Eqs. (11) and (12). This will still be a reasonable approximation if the τ do not vary by much between sensors. The latter assumption of scaling of noise equivalent power with respect to a reference sensor according to Eq. (5) is a fundamental assumption for the analysis in Sec. III.C. For the analysis in Sec. III.B it was simply convenient to do so because we have not yet verified the noise equivalent power for each prototype sensor as it will depend on the actual electronics that will be used, which is still under development, and on the noise in the experimental situation, predictions of which still need to improve. If simulations or measurements of noise equivalent power were available for different sensor incarnations, these could readily be used in the analysis in Sec. III.B.

A number of further considerations about the noise-equivalent power need to be discussed. As indicated at Eq. (6), for the illustrations in this paper [in particular Figs. 4(a) and 5, and some curves in Fig. 6] the expected attenuation of the signal for a certain frequency was equated to a noise equivalent power characteristic in the narrow bandwidth without quantifying the bandwidth. It should be stressed that this is not a limitation of the methodology, but due to the available characterization of sensors. Irrespective of whether it is formally correct, it can be noted that the result still represents the correct trend of the performance and that the results are quantitatively similar to those obtained with the criterion based on the step function (by comparing the behavior with respect to ν and $1/\Delta t$). To improve on the predictions, a full quantitative noise characterization with modern digital synchronous-detection electronics[15] would be of benefit. Nevertheless, the methodology based on the frequency criterion depends on the assumption of noise being white, and thus measurements could show it to be approximately valid or even invalid. As noted in Sec. II.A, the synchronous detection technique implies that all noise except in a relatively narrow band of the spectrum is rejected. Although elements of the methodology may still be usable if the noise characteristics are more complex (such as spectrally varying and different for different channels), any analysis also involving the spectral density of the measured signals from the plasma would be much more complex than an analytical expression. Finally, equation (10), which is central to the methodology, is only strictly true if the noise of channels is uncorrelated. Usually, that is a reasonable approximation unless off-diagonal elements in the covariance matrix are dominant.

Another consideration related to noise is that the evaluation of the incident power on the sensor by means of Eq. (1) is very sensitive to the noise level in the voltage ΔU_{out} because of the time derivative in the first term of the equation. To reduce the impact of noise, which could be amplified to the extent that the derived power is not a representative estimate of the actual

power, a filter function in the time or frequency domain is usually applied when evaluating Eq. (1) numerically. The effect of the filter function is to attenuate higher frequencies in the inverse of Eq. (2). In reality, the low-pass filter function is applied to filter out the detrimental level of noise (in the time domain this corresponds to a smoothing) and thus it affects the ability to distinguish signals at high frequencies: Secs. II.D and III.B ignoring such additional filtering leads to the curves in Figs. 4 and 5 overestimating the performance at high values of $\widehat{P_{\text{rad}}}$. For the purposes of illustrating the impact of the filter function on the performance of the diagnostic it suffices to consider a simple rectangular filter function in the time domain with time width $\pm\Delta D/2$, the Fourier transform of which is $2\sin(\omega\Delta D/2)/\omega\Delta D$ (i.e. the sinc function), although in reality more sophisticated filters would be used that attenuate the side lobes. The filter function is applied to (multiplied with) $\widehat{\Delta U_{\text{out}}}$ before evaluating Eq. (1). This means that in criterion Eq. (6) the incident power on the sensor has to be higher to be measurable at high frequencies (i.e. the right-hand side divided by the amplitude of the frequency-dependent sinc filter function in the frequency domain), which propagates to division of the right-hand side of Eq. (16). The result is shown as the dot-dashed line (purple in the online version) for a representative filter function in Fig. 4(a), which indicates that the measurable frequency will be limited by the particular filter function used (200 Hz for the 10-sample average at 1 kHz sampling shown, given by the first zero of the sinc function for $D/2 = 5$ ms). This is only an illustration: the filter function must be optimized for the particular noise and signal characteristics of the experiment and system in question, which can only really be done when experimental data is available, as has been done for all operational bolometer diagnostics.[1,3] Although for these reasons there are limitations on the emitted powers of events with time scales of the order of milliseconds that can be derived from bolometer measurements, such as disruptions, disruption mitigation systems by massive gas injection or edge-localized modes (ELMs), it can be noted that the radiated energy during such fast events can be derived excellently from the bolometer measurement: integrating Eq. (1) over the time of the short event and noting that the second term is negligible if $\Delta t \ll \tau$, one obtains $E = 2C\Delta U_{\text{out}}/\alpha U_{\text{in}} = \tau\Delta U_{\text{out}}/SU_{\text{in}}$. It is clear that the measured voltage is proportional to the energy E contained in the event that reaches the sensor scaled with τ. From the line-integral energies measured by the sensors, the total radiated energy can be calculated in the same way as the power by means of weighted summation or tomographic reconstruction. This has been done for example of disruptions.[16] It demonstrates that the performance assessment of the bolometer diagnostic should also consider the derivable radiated energy where the derivation of the power is inhibited by the combination of noise level and filter function. The measurability criterion based on $\text{NEP}_f = U_{\text{noise}}/SU_{\text{in}}$ then becomes $E > \tau\text{NEP}_f$ for a particular sensor.

An important assumption to obtain analytical expressions is that the emission-profile shape is always the same, with only the magnitude (total radiated power) varying. In the examples

shown, the rather simplistic weights and signals in Table II have been used. In reality, the weights can be optimized to be representative for a range of different emission profiles. In that case, the analysis is representative within the margin with which the total radiated power of the profiles is reproduced in simulations. We have conducted a number of tests with five different profiles regarding divertor radiation, where the peak emission moves from the divertor region to the X-point with increasing Ne seeding.[17] Using the coefficients b_i of Table II, the total radiated powers varied within ±10% for the different profiles, indicating that the coefficients are not optimal. Optimizing coefficients for multiple profiles allowed to reduce this mismatch to 2–3% between the different profiles. Many more profiles than five would be needed to truly optimize the coefficients. One can conclude that the variations with profile are likely to be well within 10%, which would imply that the curves in Figs. 4 and 5 shift left or right by such an amount.

For the examples in this paper, it was assumed that $\gamma = 0.5$. Thus, with relative accuracy $\beta = 10\%$, it was assumed that $\gamma\beta = 5\%$ of the error in the derived total radiated power comes from the random properties of the noise in the line-integral power measurements, and the rest $[(1 - \gamma)\beta = 5\%]$ from the weighted sum being imperfect and any other sources of noise and uncertainties as listed in Sec. II.D. This may be a challenge, but one can note that stochastic processes per channel (e.g. random error in calibration) largely cancel out in the sum over several channels, while systematic errors do add up. Furthermore, some sources of uncertainties are likely to have negative impact and some positive, so they would add up as square root of sum of squares. The largest variability may come from the weighted sum coefficients, as is indicated by the comparison of five profiles above. However, one can always restrict the range of plasmas analyzed with one set of coefficients to match the γ and it can be noted that bolometer diagnostics on present-day devices manage to cope with the many sources of uncertainties and derive reliable total radiated powers routinely, often within 10%.

The one-dimensional Eq. (1) usually is a good approximation of the response of bolometer sensors and is routinely used in evaluating bolometer-sensor measurements.

In Sec. II.C it was argued that the analysis based on the weighted-sum approximation can also be considered to be representative for the performance of other techniques, such as from tomography, when the sum does not have a simple geometrical interpretation, or from neural networks. Thus, the choice of the weighted-sum approach should not be a restriction. However, it must be noted that the magnitude of ΔP_{rad} in Eq. (10) is expected to reduce when more lines of sight are used in the analysis (such as in the case of tomography), which must be taken into consideration. The irregular line-of-sight distribution of diagnostics on fusion experiments and the need to include prior information in tomographic reconstruction make traditional measures of reconstruction quality less representative. The accuracy of total radiated power contained in the reconstructed profile instead may be a good measure. In that case, the current analysis

method may also predict the profile reconstruction quality obtainable by tomographic reconstruction.

V. CONCLUSIONS

The performance of a bolometer diagnostic depends on design aspects and boundary conditions such as the number of lines of sight that are possible, the étendues that are possible, sensor characteristics (sensitivity and time constant) and the noise level. A methodology based on analytical expressions has been developed to predict the performance of derivation of the total power radiated by the plasma in terms of accuracy, dynamic range and time resolution. In the case of ITER, there are still aspects that are not known well, such as achievable noise level and in how far the data processing can account for various effects. Nevertheless, the methodology has allowed to optimize the ITER bolometer diagnostic design and to match the expectations with achievable measurement performance of the diagnostic in view of constraints imposed by interfacing systems and fundamental physics limits. Curves as in Figs. 4 and 5 allow a direct understanding of the achievable performance, information which has been incorporated in high-level requirement documentation for ITER. A figure such as Fig. 6, with curves representing the full range of requirements on total-radiated power requirements in different plasma regions (not just the four example curves in Fig. 6), together with the experimental characterization of various prototype bolometer sensors, makes it possible to take a quantified decision on the optimum sensor for ITER using the considerations described at the end of Sec. III.C, which in addition to measuring performance include factors such as robustness. Although the actual ITER measurement requirements are more complex than the two points in Figs. 4(a) and (b), and four curves in Fig. 6, given that also the total radiated power in other regions is to be determined (such as in the divertor and main plasma), the points indicated are representative and illustrate that the range of prototypes (sensor 1 to sensor 3) is relevant for ITER.

Section IV described many assumptions needed for the methodology based on analytical expressions and resulting limitations in detail. In this context, it is important to realize two important factors.

First, most of the assumptions made for the methodology are no limitation on the processing of measurements of a bolometer diagnostic in operational use, which will use the actual geometry, actual étendues and actual sensor calibration factors, and can use more accurate methods that weighted sum. The main consequence of assumptions not being sufficiently accurate is that the convenient analytical expressions can no longer be used and elaborate performance simulations are needed with forward and reverse models of the diagnostic.

Second, irrespective of the strict validity of all assumptions made, such as a certain level of white noise and emission profile shape, the methodology still provides valuable insights into fundamental limits of bolometer diagnostics. For example, the shape of the curves in Figs. 4

and 5 is still likely to be representative because it results from fundamental properties of the bolometer sensor [i.e. the propagation of the fundamental frequency response of the bolometer sensor Eq. (2)]. Changes in the inputs and assumptions will mainly result in a change in shape of the curves in frequency-power parameter space according to the time constant of the sensor or a translation to the left or right: if it translates to the left, the margin between expected performance and the requirement increases, whereas if it translates to the right, the margin becomes smaller or the design could become noncompliant. Thus, irrespective of the strict validity of the assumptions, the presented methodology provides a way to conceptualize the expected measuring performance of bolometer diagnostics and can aid the design of bolometer diagnostics and predict their measuring performance, as has been illustrated by the bolometer diagnostic that is being designed for ITER. For example, one can estimate how large very fast plasma events need to be and how small slowly varying events need to be to be measurable by the bolometer diagnostic. Furthermore, the methodology allows to explore the relative importance of various diagnostic features, for example by quantifying how much the curves shift or change shape when the features are varied, and can help prioritize which aspects need to be analyzed in more detail. For example, the impact of the filter function to cope with the derivative in Eq. (1) appears not to be very pronounced as described in section Sec. IV: only at high powers where it is probably better to diagnose the energy radiated by the plasma instead of the power. The methodology offers a quick way with relatively little processing to assess roughly the impact of aspects such as noise characteristics.

Regarding future work, it would be beneficial to quantify better the effect of the various assumptions, including each of the sources of uncertainties contained in the quantity γ, both to improve the performance predictions and indicate which further analysis outside the methodology should be prioritized. For example, experimental characterization of the noise magnitude and spectrum with the entire signal chain and digital electronics will be of prime interest during commissioning of the diagnostic. However, we do not see great scope for improvements to the analytical model itself. One known limitation is that Eqs. (2) and (6) only consider the amplitude – any effect from the phase shift that results from the complex transfer function has not been considered in this paper. It may be worthwhile to consider whether there is any further impact on the analysis and results from the phase shift.

In general, we hope that this methodology reenforces interest in characterizing bolometer diagnostics in more detail, with the aim of improving the fidelity of the measurements.

ACKNOWLEDGEMENTS

AUTHOR DECLARATIONS

Conflict of Interest

The authors have no conflicts to disclose.

Author Contributions

L.C. Ingesson Conceptualization (lead); methodology (lead); software (lead); validation (equal); visualization (lead); writing – original draft (lead). **A. Doblas** Visualization (supporting); writing – review and editing (supporting). **A. Gandhi** Methodology (supporting); software (supporting); visualization (supporting); writing – review and editing (supporting). **S. Jahanbakhsh** Investigation (equal); writing – review and editing (supporting). **H. Meister** Conceptualization (supporting); methodology (supporting); investigation (equal); validation (equal); writing – review and editing (supporting).

DATA AVAILABILITY

The data that support the findings of this study are available from the corresponding author upon reasonable request.

REFERENCES

[1]   L.C. Ingesson, B. Alper, B.J. Peterson, and J.-C. Vallet, "Chapter 7: Tomography diagnostics – bolometry and soft x-ray detection," Fusion Sci. Technol. **53**, 528 (2008); http://dx.doi.org/10.13182/FST53-528

[2]   H. Meister, M. Bernert, W. Biel, M. Han, L.C. Ingesson, K. Mukai, F. Penzel, B.J. Peterson, R. Reichle, M.L. Reinke, S. Schmitt, and D. Zhang, "Bolometer developments in diagnostics for magnetic confinement fusion," J. Inst. **14**, C10004 (2019); https://doi.org/10.1088/1748-0221/14/10/C10004.

3   A.J.H. Donné, A.E. Costley, R. Barnsley, H. Bindslev, R. Boivin, G. Conway, R. Fisher, R. Giannella, H. Hartfuss, M.G. von Hellermann, E. Hodgson, L.C. Ingesson, K. Itami, D. Johnson, Y. Kawano, T. Kondoh, A. Krasilnikov, Y. Kusama, A. Litnovsky, P. Lotte, P. Nielsen, T. Nishitani, F. Orsitto, B. Peterson, G. Razdobarin, J. Sanchez, M. Sasao, T. Sugie, G. Vayakis, V. Voitsenya, K. Vukolov, C. Walker, K. Young, and ITPA Topical Group on Diagnostics, "Progress in the ITER Physics Basis – Chapter 7: Diagnostics," Nucl. Fusion **47**, S337 (2007); https://doi.org/10.1088/0029-5515/47/6/S07

4   K. Young, "Chapter 1: Plasma measurements: an overview of requirements and status," Fusion Sci. Technol. **53**, 281 (2008); https://doi.org/10.13182/FST08-A1673

5   H. Meister, F. Penzel, Z. Szabo-Balint, R. Reichle, and L.C. Ingesson, "Performance estimations for the ITER bolometer diagnostic," Fusion Eng. Design **146**, 1015 (2019); https://doi.org/10.1016/j.fusengdes.2019.01.146

6   K.F. Mast, J.C. Vallet, C. Andelfinger, P.Betzler , and G. Schramm. "A Low Noise Highly Integrated Bolometer Array for Absolute Measurement of VUV and Soft X Radiation," Rev. Sci. Instrum. **62**, 744 (1991); https://doi.org/10.1063/1.1142078

7   E.R. Müller, G. Weber, F. Mast, G. Schramm, E. Buchelt, and C. Andelfinger, *Design of a four-channel bolometer module for ASDEX Upgrade and Tore Supra* (Report IPP 1/224, 1985)

8   S. Jahanbakhsh, J.D. Hare, H. Meister, L.C. Ingesson, M. Majewski, F. Penzel, S. Schmitt, U. Walach, and M. Dubois, Rev. Sci. Instrum. **94**, 033503 (2023); https://doi.org/10.1063/5.0134449

9   L. C. Ingesson, C. F. Maggi, and R. Reichle, "Characterization of geometrical detection-system properties for two-dimensional tomography", Rev. Sci. Instrum. **71**(3), 1370 (2000); https://doi.org/10.1063/1.1150466

10   M. Maraschek, J. C. Fuchs, K. F. Mast, V. Mertens, and H. Zohm, "Real-Time Determination of Total Radiated Power by Bolometric Cameras with Statistical Methods," Rev. Sci. Instrum. **69**, 109 (1998); https://doi.org/10.1063/1.1148485

11   P.L. van de Giessen, G. Kawamura, S. Borling, K. Mukai and B.J. Peterson, "Development of a weighted sum estimate of the total radiated power from large helical device plasma." Rev. Sci. Instrum. **92**, 033518 (2021); https://doi.org/10.1063/5.0027302

12   L.C. Ingesson, *Comparison of Methods to Determine the Total Radiated Power in JET* (Report JET-R(99)06, JET Joint Undertaking, Abingdon, 1999) https://scipub.euro-

fusion.org/archives/jet-archive/comparison-of-methods-to-determine-the-total-radiated-power-in-jet or https://scipub.euro-fusion.org/wp-content/uploads/2014/11/JETR99006.pdf

13 O. Barana, A. Murari, P. Franz, L. C. Ingesson, and G. Manduchi, "Neural Networks for Real Time Determination of Radiated Power in JET," Rev. Sci. Instrum. **73**, 2038 (2002); https://doi.org/10.1063/1.1463714

14 H. Meister, W. Kasparek, D. Zhang, M. Hirsch, J. Koll, and A. Zeitler, "Millimetre wave attenuation of prototype diagnostic components for the ITER bolometers," Fusion Eng. Design **96–97**, 861 (2015); https://doi.org/10.1016/j.fusengdes.2015.06.021

15 J. Lovell, G. Naylor, A. Field, P. Drewelow, R. Sharples and JET Contributors, "An FPGA-based bolometer for the MAST-Upgrade Super-X Divertor", Rev. Sci. Instrum. **87**, 11E721 (2016); https://doi.org/10.1063/1.4961556

16 V. Riccardo, P. Andrew, L.C. Ingesson and G. Maddaluno, "Disruption heat loads on the JET MkIIGB divertor," Plasma Phys. Control. Fusion **44**, 905 (2002); https://doi.org/10.1088/0741-3335/44/6/319

17 J.D. Lore, X. Bonnin, J.-S. Park, R.A. Pitts and P.C. Stangeby, "High gas throughput SOLPS-ITER simulations extending the ITER database to strong detachment," Nucl. Fusion **62**, 106017 (2022); https://doi.org/10.1088/1741-4326/ac8a5f

Noise density level U_{noise}'

$\hat{\Delta U}_{out}'$ (V/Hz)

$1/2\pi\tau$

Frequency ν (Hz)

Noise level U_{noise}

$\hat{\Delta U}_{out}$ (V)

t_1 $t_1 + \Delta t$ $t_1 + \tau$

Time $t \rightarrow$

(a)

(b)